Research article

Ranran Zhang, Qiuling Zhao, Xia Wang*, Wensheng Gao, Jensen Li and Wing Yim Tam*

Measuring circular phase-dichroism of chiral metasurface

https://doi.org/10.1515/nanoph-2019-0061
Received February 27, 2019; revised April 1, 2019; accepted April 5, 2019

Abstract: The ability of chiral media to differentiate circularly polarized light is conventionally characterized by circular dichroism (CD) which is based on the difference in the absorption of the incident light for different polarizations. Thus, CD probes the bulk properties of chiral media. Here, we introduce a new approach termed as circular phase-dichroism that is based on the surface properties and is defined as the difference of the reflection phase for different circularly polarized incident lights in characterizing chiral media. As a demonstration, we measure the reflection phase from planar chiral sawtooth metasurface for circularly polarized light in the visible range using a simple Fabry Perot interference technique. The measured circular phase-dichroism is also crosschecked by conventional CD measurement of the transmitted light and by full-wave simulations. Our results demonstrate the potential applications of circular phase-dichroism in sensing and metasurface characterizations.

Keywords: chiral media; circular dichroism; phase measurement; circular phase-dichroism.

***Corresponding authors: Xia Wang,** Optoelectronic Materials and Technologies Engineering Laboratory, Shandong, Physics Department, QingDao University of Science and Technology, QingDao, China, e-mail: phwangxia@163.com; and **Wing Yim Tam**, Optoelectronic Materials and Technologies Engineering Laboratory, Shandong, Physics Department, QingDao University of Science and Technology, QingDao, China; and Department of Physics and William Mong Institute of Nano Science and Technology, Hong Kong University of Science and Technology, Clear Water Bay, Kowloon, Hong Kong, China, e-mail: phtam@ust.hk.
https://orcid.org/0000-0002-5275-626X
Ranran Zhang: Optoelectronic Materials and Technologies Engineering Laboratory, Shandong, Physics Department, QingDao University of Science and Technology, QingDao, China; and Department of Physics and William Mong Institute of Nano Science and Technology, Hong Kong University of Science and Technology, Clear Water Bay, Kowloon, Hong Kong, China
Qiuling Zhao: Optoelectronic Materials and Technologies Engineering Laboratory, Shandong, Physics Department, QingDao University of Science and Technology, QingDao, China
Wensheng Gao and Jensen Li: Department of Physics and William Mong Institute of Nano Science and Technology, Hong Kong University of Science and Technology, Clear Water Bay, Kowloon, Hong Kong, China

1 Introduction

Metamaterials are man-made structures with sizes much smaller than the wavelengths of interest [1–3]. Novel properties such as negative refraction [4, 5], superlens [6], and cloaking [7] that are not feasible using natural materials can be realized because of the structural effects of metamaterials. Due to the advances in nanotechnologies, metamaterials can now be fabricated to achieve the above properties towards optical frequencies [8–10]. On the other hand, two-dimensional (2D) metasurface, being a subset of metamaterials, has high potential for device applications such as beam deflectors [11, 12], metalenses [13], optical vortex plates [14, 15], cloaking surfaces [16], metaholograms [17, 18], etc. due to its simplicity in fabrication and large-scale production, and thus has drawn much interest recently. Recent review articles on metasurfaces summarize well the fundamentals and potential applications of metasurfaces [19–22].

Ordinary materials are not sensitive to the handedness of incident light and thus they are labeled as achiral. On the contrary, chiral materials exhibit novel optical activities such that the handedness of incident light can be modified or transformed [23, 24]. Optical devices made of natural chiral materials have weak optical activities and thus they are usually very bulky in order to achieve noticeable chiral effects. This drawback is circumvented by the use of micro/nanometer-thick chiral metasurfaces in which large optical activities (polarization rotation and circular dichroism) are possible [25–43]. Chiral property is conventionally characterized, other than the polarization rotation, by the circular dichroism (CD) defined as the difference in the absorption/transmission of different circularly polarized, left- and right-handed, incident light [23, 24]. However, as CD probes the bulk properties

of the chiral materials, the CD signal thus depends on the sample size. This size dependence could reduce its sensitivity for highly absorptive materials, e.g. metals, in the visible range. Moreover, current metasurfaces are mostly metallic based. Thus, it is highly desirable to characterize chiral metasurfaces, especially metallic based metasurfaces, by probing the surface properties like reflection or more sensitively the reflection phase.

The reflection phase of a metasurface can be obtained using standard interference method for single or discrete wavelength(s). However, it is only recently that reflection phase is obtained over a wide range in the optical wavelengths using a simple Fabry Perot (FP) interference technique [44, 45] and a cross-polarization method [46]. The FP method has been applied recently in obtaining the reflection phase, and hence the Zak phase, at the photonic bandgaps [47, 48] as well as in the photonic bands [49], using an effective medium approach, of 1D photonic crystals for unpolarized incident light in the optical range. The FP technique can be extended to reflection phase of chiral metasurface using circularly polarized incident light.

Here we propose a new approach in the characterization of chiral metasurfaces using circular phase-dichroism based on the reflection phase of circularly polarized incident light of different handedness. The circular phase-dichroism is realized in the visible range using planar chiral metasurfaces consisting of hundred nanometer thick complementary Au sawtooth nanoarrays fabricated using simple e-beam direct write and e-beam vapor deposition techniques. The measured circular phase-dichroism is comparable to the conventional CD measurements of transmissions of left-handed (LCP) and right-handed (RCP) circularly polarized incident light. We also perform full-wave simulations for the chiral Au sawtooth metasurfaces and obtain good qualitative agreement with the experiment. Our results demonstrate the potential applications of circular phase-dichroism in sensing and metasurface characterizations.

2 Reflection phase by Fabry Perot interferometry

We chose a transmission etalon configuration as shown in Figure 1A for our reflection phase measurement using a Fabry Perot interference technique. A glass window is placed above a metasurface sample to form a glass-air-metasurface etalon. Circularly polarized incident light (beam 0) from below first passes the metasurface,

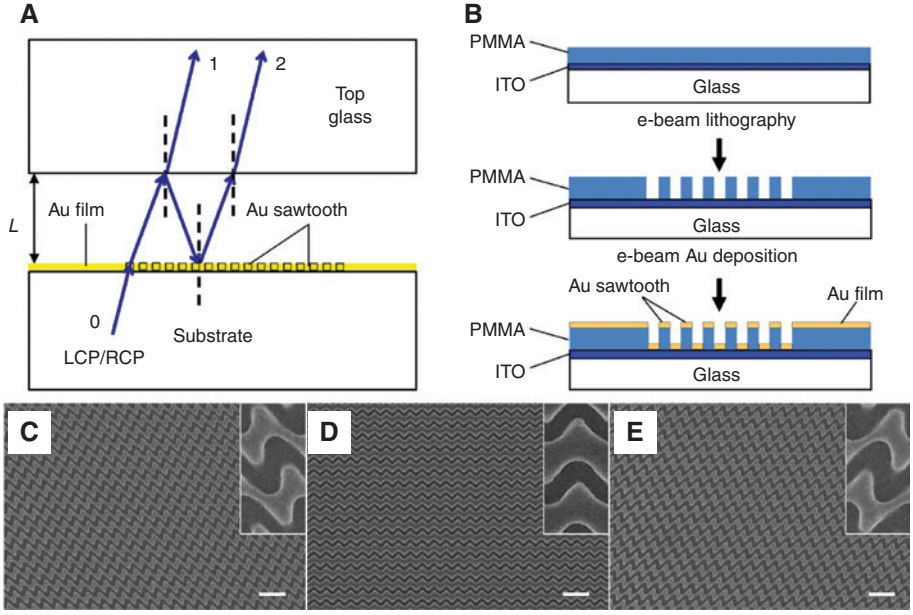

Figure 1: Phase measurement and fabrication of complementary Au sawtooth metasurface.
(A) Schematic for the measurement of reflection phase using transmission of circularly polarized, LCP/RCP, incidence light. (B) Fabrication procedures of complementary Au sawtooth metasurface. (C)–(E) SEM images of **N**-, **V**- and **И**-type sawtooth metasurfaces, respectively. The white scale bars are 1 μm. The width of the Au sawtooth on the bottom layer is about 135 nm for the vertical bar and 110 nm for the slanted bar for the **N**- and **И**-type sawtooth metasurfaces while it is about 120 nm for both slanted arms of the **V**-type sawtooth metasurface. Insets are enlarged images of the Au sawtooth unit cells.

then part of the beam is transmitted through the top glass (beam 1, amplitude E_1) and the remaining beam gets reflected backward from the top glass surface to the sample. The backward beam is then reflected by the sample and then transmitted through the top glass (beam 2, amplitude E_2) to interfere with beam 1. Neglecting higher order reflections inside the etalon, the interference of beams 1 and 2 produces oscillations with peaks and troughs in the transmittance T (for normal incidence $T = E_1^2 + E_2^2 + 2E_1E_2\cos(2kL + \phi_G + \phi_S)$ where ϕ_G/ϕ_S is the reflection phase of the top-glass/sample from air). The condition for constructive interference of the transmittance (for the peaks) satisfies the following equation:

$$2kL + \phi_G + \phi_S = 2m\pi, \tag{1}$$

where $k = 2\pi/\lambda_m$ with λ_m the wavelength of the mth peak interference order and $\phi_G = \pi$. (For destructive interference, i.e. transmission troughs, a π is added to the right-hand-side of Eq. (1). Furthermore, for non-dispersive media, the condition for constructive interference given by Eq. (1) for the two-beam model agrees with the one obtained by the multi-beam model counting all the reflections inside the glass-air-metasurface etalon, independent of the difference in the overall transmittance for the two models. Moreover, the correction due to dispersion is also small as the FP oscillations also come from the $\cos(2kL + \phi_G + \phi_S)$ term in the multi-beam model.) From Eq. (1), the reflection phase for different handedness incident light can be calculated once the air-gap spacing L is obtained from the slope of a linear fit to a plot of m vs. $(1/\lambda_m)$ [44, 45]. Finally, the circular phase-dichroism can be obtained as the reflection phase difference, between the LCP and RCP incident light, i.e. $\Delta\phi = \phi_{\mathrm{RCP}} - \phi_{\mathrm{LCP}}$.

3 Experiment

3.1 Fabrication of complementary Au sawtooth nanoarray metasurface

Our planar metasurface consists of complementary Au sawtooth nanoarrays. Figure 1B shows the fabrication procedures, similar to those reported earlier [36, 37], of the complementary Au sawtooth nanoarray metasurfaces. About 180 nm PMMA was first spin-coated onto indium-tin-oxide (ITO) glass substrate (65 nm ITO and 1 mm glass), and then an e-beam (Raith e-LiNE) was used to write sawtooth nanoarray patterns, size $200 \times 200\ \mu m^2$ and ~100–130 nm for the width of the sawtooth array, onto the PMMA. After developing the PMMA into sawtooth hole nanoarrays, a layer of ~30 nm Au was deposited at normal incidence, using an e-beam evaporator, onto the patterned as well as the non-patterned areas producing complementary, top hole and bottom solid, Au sawtooth nanoarrays as well as simple Au film. Three complementary Au sawtooth nanoarray metasurfaces, namely **N**-, **V**- and **И**-types, were fabricated as shown in Figure 1C–E, respectively. The insets show the unit cells for the different type of sawtooth nanoarrays. As the sawtooth **N**/**И** "atom" breaks the mirror symmetry, the **N**-/**И**-type metasurfaces are thus planar (2D) chiral while the **V** "atom" preserves the mirror symmetry and thus the **V**-type metasurface is achiral. The Au sawtooth metasurfaces have 450 nm lattice spacing in both horizontal and vertical directions. Note that except the **V**-type, both the **N**- and **И**-type Au sawtooth metasurfaces have half-lattice, i.e. 225 nm, horizontal shift between alternate rows so that each Au sawtooth nanoarray is disconnected from the above and below neighboring sawtooth nanoarrays as shown in Figure 1C and E.

3.2 Optical measurement and circular dichroism

We first characterize the chiral complementary Au sawtooth metasurfaces by the conventional CD measurements. We used a simple setup consisting of a polarizer and a super-achromatic quarter waveplate (APSAW-5 from Astropribor) as reported before [36] to generate circularly polarized light covering 480–850 nm visible range. Spectral measurement of transmission for left-circularly (LCP) and right-circularly (RCP) polarized light incident from below, through the ITO glass substrate, with the sample facing upward was performed by an Ocean Optics USB4000 spectrometer connected, using an optical fiber, to an optical microscope with a 5X objective covering a $\sim 100 \times 100\ \mu m^2$ area. Figure 2A–C show the transmittance of LCP (red curves) and RCP (blue curves) for the **N**-, **V**- and **И**-type complementary Au sawtooth metasurfaces, respectively. The LCP and RCP transmittance are clearly different for the **N**- and **И**- type Au sawtooth metasurfaces while they are nearly the same, within the experimental errors, for the **V**-type Au sawtooth metasurface. Thus the **N**- and **И**-type Au sawtooth metasurfaces are chiral while the **V**-type Au sawtooth metasurface is achiral. Importantly, the transmittance is almost reciprocal for LCP and RCP between the **N**- and **И**-type Au sawtooth metasurfaces, demonstrating well the anti-symmetric chiral property of 2D chiral materials [26, 29, 30] and the quality of our samples. In contrast, Figure 2B shows almost identical

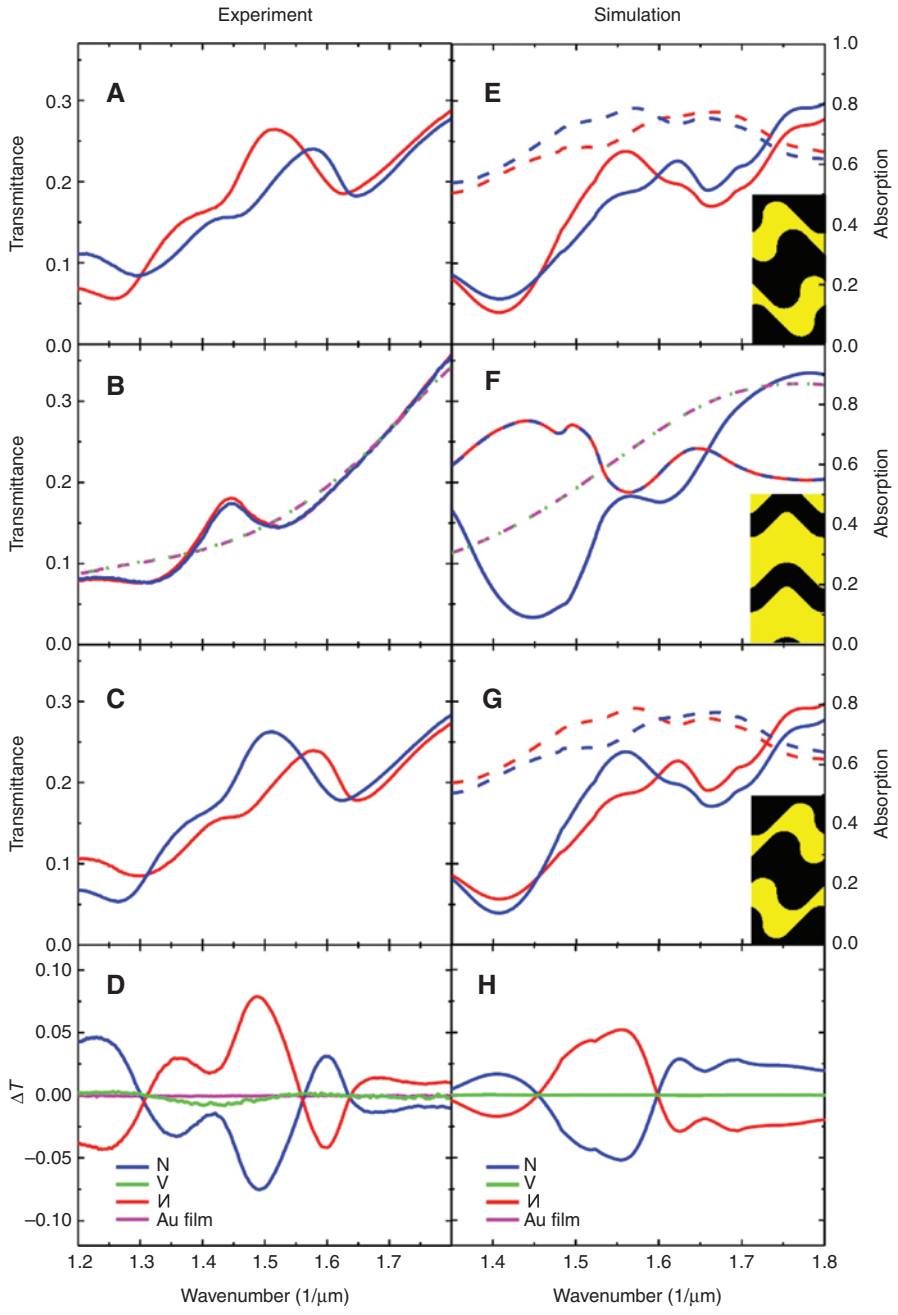

Figure 2: Transmittance and circular dichroism of complementary Au sawtooth metasurface.
Transmittance of LCP (solid red curves) and RCP (solid blue curves) incidence light for (A) **N**-, (B) **V**- and (C) **И**-type complementary Au sawtooth metasurfaces. The magenta (LCP) and green (RCP) dashed curves in (B) are transmittance for Au film with no structure. (D) The transmission difference (CD) of $T_{RCP} - T_{LCP}$. (E)–(H) Corresponding results from CST simulations. The red/blue dashed curves in (E)–(G) are the absorptions for LCP/RCP incident light. Parameters for the simulations: thickness: Au 30 nm, PMMA 180 nm, ITO 65 nm, substrate glass 1 mm; sawtooth width (bottom layer): **N**- and **И**-type sawtooth metasurfaces – vertical bar 135 nm, slanted bar 110 nm, and **V**-type sawtooth metasurface slanted bars 120 nm. The insets show the unit cells used in the simulations. The gold color represents the top Au layer and the black is the bottom Au layer.

transmittance for LCP (red curve) and RCP (blue curve) for the **V**-type Au sawtooth metasurface, as well as the Au film (magenta and green dashed curves), as they are achiral.

We approximate the circular dichroism (CD) by the transmission difference ($\Delta T = T_{RCP} - T_{LCP}$) as shown in Figure 2D. CD values, as high as ~0.075 at wave number 1.49 μm^{-1}, are observed at resonances associated with different absorptions in the Au sawtooth metasurfaces. Note also that the CDs for the **N**- and **И**-type Au sawtooth metasurface are almost anti-symmetricwhile it is almost zero

for the **V**-type Au sawtooth metasurface, as well as the Au film. The transmittance of LCP incident light is slightly red-shifted with respect to that of RCP incident light for **N**-type Au sawtooth metasurface as shown in Figure 2A. It is reversed for the **И**-type Au sawtooth metasurface as shown in Figure 2C. This could be explained by the different losses of metasurfaces as shown in the simulations below.

3.3 Reflection phase

Figure 1A shows the schematic for the phase measurement setup for the glass-air-sawtooth etalon consisting of a top glass window placed above an Au sawtooth metasurface with an air-gap ($L \sim 10$ μm) fixed by spacers between the top glass and the sample. We obtained the transmission of the glass-air-sawtooth etalon using the procedures as used for the CD measurements above. Figure 3A shows the transmittance for the glass-air-Au film etalon (green curve) and also the glass-air-sawtooth (**V**-type) etalon (red curve) showing clearly peaks and troughs as expected from the FP interference. Figure 3B shows a plot of transmission interference order m vs. the corresponding wave number $1/\lambda_m$ (blue circles) for the glass-air-Au film etalon (green curve) in Figure 3A. The data is well fitted by a linear relation, red line in Figure 3B, despite small

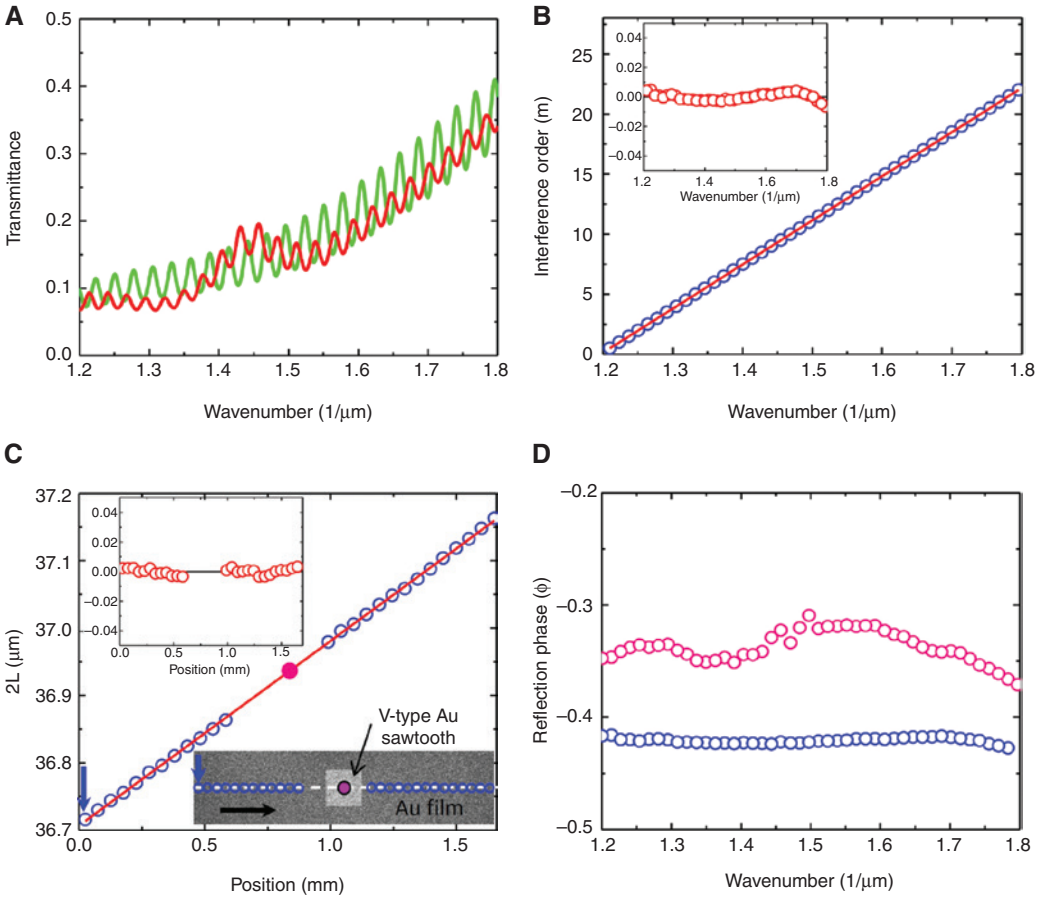

Figure 3: Reflection phase measurement.
(A) FP transmission of RCP incidence light for Au film (green curve) and **V**-type Au sawtooth metasurface (red curve). (B) Interference order m vs the corresponding $1/\lambda_m$ for the Au film in (A). Open blue circles are the data and the solid red line is a fit to the data using Eq. (1). The inset shows the residual of the fit. (C) The slope ($2L$) obtained from the m vs. $1/\lambda_m$ fit for Au film taken at different positions (open blue circles) along a path (white dashed line in the lower-right SEM image inset) crossing over the **V**-type Au sawtooth metasurface. The blue arrow indicates the first position of the Au film where data was taken for the reflectance shown in (A). The red line is a linear fit to the data. The upper-left inset is the residual of the fit. The solid pink dot is the interpolated air-gap at the **V**-type sawtooth metasurface. The lower-right inset shows a SEM image of the **V**-type Au sawtooth metasurface (light grey 200×200 μm^2 square) and the Au film (dark grey). The open circles are positions where measurements were carried out with the first position indicated by the blue arrow. The horizontal black arrow indicates the direction of measurements. (D) Open blue and pink circles are the reflection phase of RCP incidence for the Au film at the position indicated by the blue arrow shown in (C) and the **V**-shaped Au sawtooth metasurface, respectively.

systematic deviations due to numerical aperture effect from the microscope objective [45]. The quality of the fit is better displayed in the residual of the fit, less than 1% over the whole range, as shown in the inset. From the fit, we can then obtain the air-gap spacing and the reflection phase of the Au film.

To obtain the reflection phase of the Au sawtooth metasurfaces, we measure the air-gap spacing of the glass-air-sawtooth etalon at various locations across the sample as indicated by the path (white dashed line) shown in the lower-right SEM image inset of Figure 3C by starting from a non-patterned area (Au film), passing over the patterned sawtooth area, and ending at another non-patterned area (Au film again) on the opposite side of the Au sawtooth metasurface. Thus, the air-gap spacing right above the Au sawtooth metasurface can be obtained by interpolating the results of the Au film areas. Figure 3C shows the slope ($2L$), hence the air-gap spacing, of a glass-air-sawtooth (**V**-type) etalon, taken at different Au film locations corresponding to those labeled (blue circles) in the lower-right SEM image inset. A straight line (in red) fits the data very well as shown in the inset for the residual of the fit. The pink solid dot in Figure 3C is the interpolated slope (hence the air-gap spacing) for the **V**-type Au sawtooth metasurface. Knowing the air-gap spacing, the reflection phase (chosen from –1 to 0 after normalized by 2π) can now be calculated using Eq. (1) and the peak/trough wave numbers of the transmittance for the **V**-type Au sawtooth metasurface shown as red curve in Figure 3A. The result is shown in Figure 3D as pink circles for RCP incident light. The variations of reflection phase with wavelength are related to the resonances of the **V**-type Au sawtooth metasurface [36]. In contrast, the reflection phase of the Au film (blue circles) is relatively featureless as shown in Figure 3D obtained at the first Au film location indicated by the blue arrow in Figure 3C. Measurements at other Au film locations along the white dashed line in the lower-right SEM inset are the same within the scatters. Note that the reflection phase has not been corrected for numerical aperture effects coming from the microscope objective and the optical fiber [45] as we are interested only in the relative phase of the Au sawtooth metasurface with respect to the Au film or between different incident polarizations, LCP and RCP.

Figure 4A–C show the transmittance of LCP (red curves) and RCP (blue curves) incident light for the glass-air-sawtooth etalons with the **N**-, **V**- and **И**-type complementary Au sawtooth metasurfaces, respectively. The

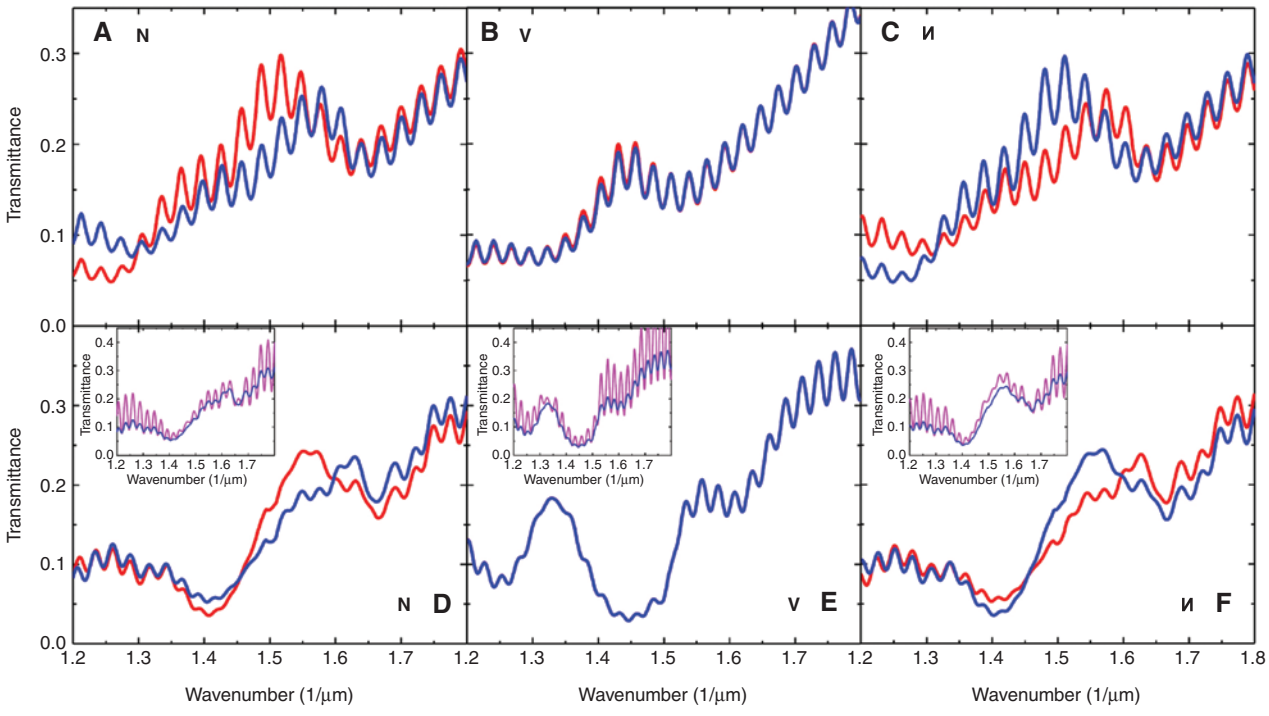

Figure 4: Transmittance of glass-air-metasurface etalon.
Transmittance of glass-air-Au sawtooth etalon for LCP (solid red curves) and RCP (solid blue curves) incidence light for (A) **N**-, (B) **V**- and (C) **И**-type complementary Au sawtooth metasurface, respectively. (D)–(F) Corresponding results from CST simulations using $r_G = 0.2$. The insets show the transmittance calculated using $r_G = 0.2$ (blue curves) and 1.0 (purple curves) for RCP incidence.

transmittances for the metasurface etalons follow the same trends for the sawtooth samples without the top glass as shown in Figure 2A–C. Figure 5A–C show the reflection phase with respect to Au film for the **N**-, **V**- and **И**-type complementary Au sawtooth metasurfaces, respectively, for LCP (red circles) and RCP (blue circles) incident light obtained using the method as stated in the above paragraph. Note that the reflection phase for the **V**-type Au sawtooth metasurface is the same for LCP and RCP incident light as shown in Figure 5B, in good analogy to that of the transmittance in the CD measurements shown in Figure 2B as the **V**-type Au sawtooth metasurface is

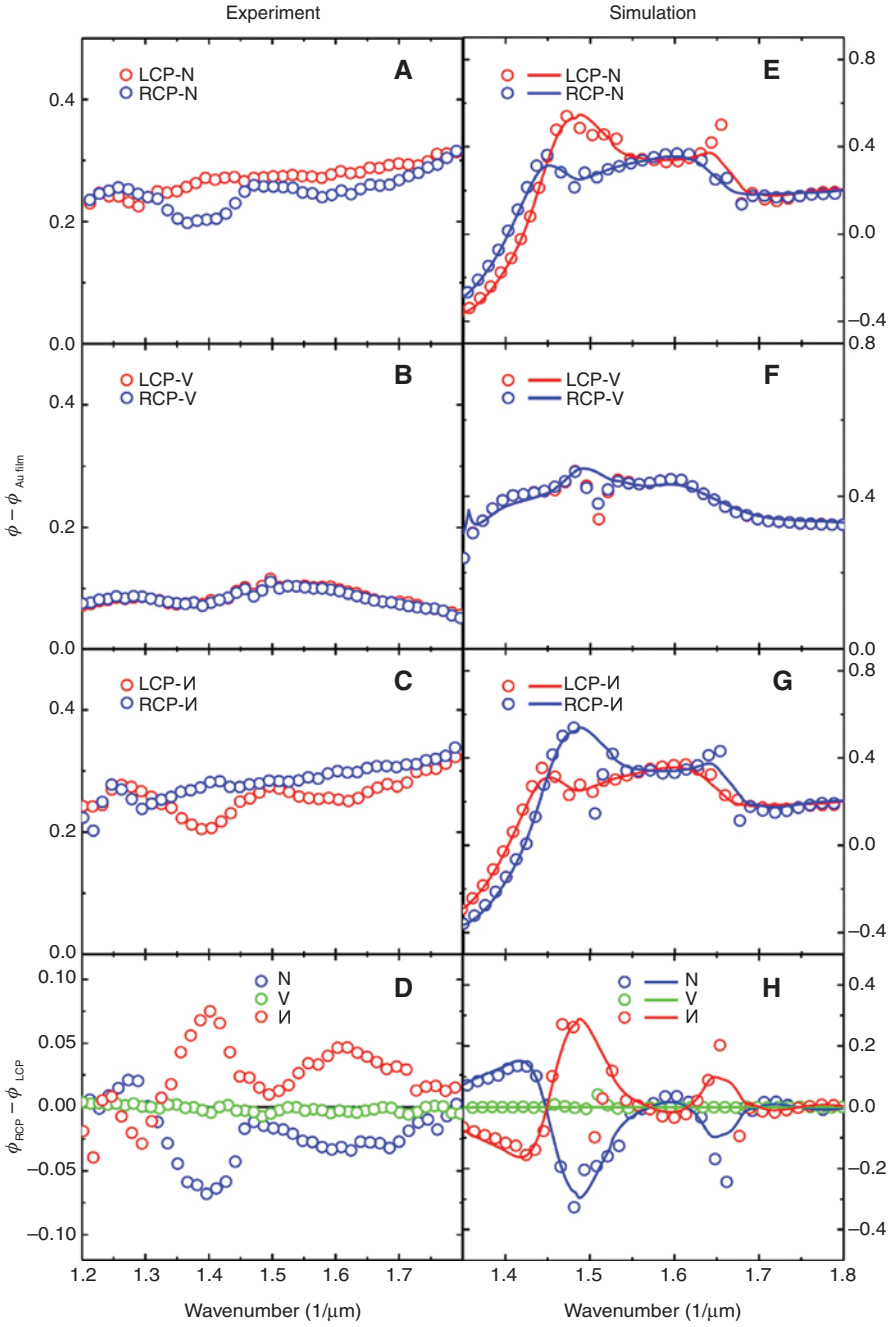

Figure 5: Reflection phase and circular phase-dichroism.
(A)–(C) Reflection phase of LCP (red circles) and RCP (blue (circles) incidence light with respect to Au film, i.e. $\phi - \phi_{Au\ film}$, for **N**- (blue circles), **V**- (green circles) and **И**-type (red circles) complementary Au sawtooth metasurfaces, respectively. (D) Reflection phase difference, $\phi_{RCP} - \phi_{LCP}$, for **И**- (blue circles), **V**- (green circles) and **И**-type (red circles) complementary Au sawtooth metasurfaces. (E)–(H) Corresponding results from CST simulations using $r_G = 0.2$. Symbols are results obtained using the peak/trough fitting method and solid curves are calculated using Eq. (5).

achiral. In contrast, the **N**- and **И**-type complementary Au sawtooth metasurfaces, Figure 5A and C, show almost opposite results for LCP and RCP incident light, also in good analogy to those of the CD measurements shown in Figure 2A and C.

The chirality of the metasurface can now be expressed in terms of the circular phase-dichroism defined above as $\Delta\phi = \phi_{RCP} - \phi_{LCP}$. Figure 5D shows the results of the circular phase-dichroism for the complementary Au sawtooth metasurfaces. The circular phase-dichroism is almost opposite for the **N**- (blue circles) and **И**-type (red circles) complementary Au sawtooth metasurfaces, in good correspondence with the CD measurements. Note also, that the values can be as high as ~0.08 at 1.4 μm^{-1}, comparable to the CD measurements shown in Figure 2D. However, it is nearly zero, within the noise, for the achiral **V**-type complementary Au sawtooth metasurface, green circles in Figure 5D, in perfect agreement with the CD measurement in Figure 2D for the **V**-type Au sawtooth metasurface. The above results demonstrate well that our approach of using circular phase-dichroism is as good as the conventional CD measurement in the characterization of chiral materials. Note that the chiral phase-dichroism in Figure 5D resembles the CD in Figure 2D very much and thus it would be interesting to explore their correlations.

4 Model of complementary Au sawtooth nanoarray metasurface

4.1 Full-wave simulation

In order to support our approach in characterizing chiral materials using the circular phase-dichroism we perform full-wave simulations for our glass-air-metasurface etalon system. We use a finite-integration-technique simulator from CST Microwave Studio to model the complementary Au sawtooth nanoarray metasurfaces with unit cells, insets in Figure 2E–G, constructed to resemble those shown in Figure 1C–E for the experiments as closely as possible using the software of the simulator. The transmittance of the Au sawtooth metasurface is calculated using normal incidence circularly polarized light. We use periodic boundary conditions and the extracted dispersion for Au film reported in Refs. [50, 51], with larger imaginary part to accord for higher losses, for our simulations. Standard dispersions for ITO [51], glass [52], and PMMA [53] are used in the simulations. To reduce artifacts due to finite mesh and interpolation of dispersion parameters used in the simulations, we smooth the results over a range of ~0.04 μm^{-1} in wave number. Small variations of the physical parameters, e.g. the PMMA thickness, the widths and the turns of the Au sawtooth metasurfaces, do not change the results much.

4.2 Transmittance and circular dichroism

Figure 2E–G show the simulated transmittance, red curves for LCP and blue curves for RCP incident light, for the **N**-, **V**- and **И**-type complementary Au sawtooth metasurfaces, respectively. It is clear that the transmittance is different for the LCP and RCP incidence for the **N**- and **И**-type chiral Au sawtooth metasurfaces while it is the same for the achiral **V**-type Au sawtooth metasurface. Moreover, the simulations reproduce similar transmittance shifts of LCP with respect to that of RCP incident light for the **N**- and **И**-type Au sawtooth metasurfaces as observed in the experiment, Figure 2A and C. Also displayed in Figure 2E–G are the absorptions, red (LCP incidence) and blue (RCP incidence) dashed curves, obtained by $A = 1 - R$(reflectance) – T(transmittance) for the complementary Au sawtooth metasurfaces. Overall, the absorptions show opposite trends as the transmittance for the chiral **N**- and **И**-type Au sawtooth metasurfaces while they are the same for the achiral **V**-type Au sawtooth. Since absorption is related to the dissipation resulted from the current flow on the metal surfaces due to resonances of the Au sawtooth metasurface, thus the larger the current flow the higher the absorption. As the **N**- and **И**-type Au sawtooth metasurfaces are chiral, the strength of the resonances will then depend on the handedness of the incident light. Take the minimum CD at wave number ~1.56 μm^{-1} for the **N**-type Au sawtooth metasurface as an example. The simulation shows that overall, the strength of the resonances for RCP incidence is larger than that of LCP for wave numbers below ~1.6 μm^{-1}, resulting in higher absorption for RCP (blue dashed curve) than LCP (red dashed curve) as shown in Figure 2E. Furthermore, as there is a dip in the absorption for LCP incidence at ~1.54 μm^{-1}, the LCP transmittance reaches a maximum at ~1.55 μm^{-1} while the RCP transmittance is more the less flat in this wave number range as shown in Figure 2E. The combined effects lead to a minimum CD at ~1.56 μm^{-1} as shown in Figure 2H for the **N**-type Au sawtooth metasurface. The above scenario is reversed for the **И**-type Au sawtooth metasurface, Figure 2G and H. Importantly, the simulations reproduce the characteristic features as observed in the experiment for wave numbers between 1.2 μm^{-1} and ~1.6 μm^{-1} despite

a shift in the wave number, e.g. the transmittance crossings ($T_{LCP} = T_{RCP}$) at ~1.3 μm^{-1} and ~1.55 μm^{-1} observed in the experiment are now at ~1.45 μm^{-1} and ~1.6 μm^{-1} respectively, for the simulations. These shifts are possibly due to the uncertainties in the dispersions, the physical parameters and also the effect of the ITO substrate glass. Moreover, there is discrepancy at wave numbers > 1.6 μm^{-1} where the transmittance crossing at 1.63 μm^{-1} observed in the experiment, Figure 2A and C, cannot be reproduced in the simulations. This discrepancy could be due to larger uncertainties of the dispersions at short wave lengths. Figure 2H shows the circular dichroism (transmission difference) of the simulated results showing very similar behavior as the experiment, except the CD troughs/peaks at ~1.35 μm^{-1} and 1.48 μm^{-1} observed in the experiment for the **N**-/**И**- type chiral Au sawtooth metasurface are now merged together as a broad trough/peak from ~1.48 μm^{-1} to ~1.56 μm^{-1} in the simulation. Overall, the model captures the prominent features and agrees qualitatively with the experiment. Better agreement could be obtained by importing directly, the SEM images of the unit cells as shown in the insets of Figure 1C–E to the CST simulator, or by fine tuning the physical parameters used in the simulations, and/or averaging over many simulations using slightly different parameters to account for the variations in the Au sawtooth nanoarrays.

4.3 Reflection phase

The glass-air-sawtooth system shown in Figure 1A is too large for the CST simulator as it covers nano-scale of the Au film up to millimeter-scale of the air gap and top glass. Thus we first obtain the reflection and transmission coefficients for the Au film (r_{ij}^{Au} and t_{ij}^{Au}) and Au sawtooth metasurface (r_{ij}^{S} and t_{ij}^{S}) for circularly polarized incident beam $j=\pm$ and reflected/transmitted beam $i=\pm$ from simulations without the top glass. (Here + is defined for RCP and − for LCP.) We then use a two-beam interference model as shown in Figure 1A to calculate the transmittance of the glass-air-sawtooth etalon. As the **N**- and **И**-type Au sawtooth metasurfaces are chiral, for any circularly polarized incident light there will be co-polarization (t_{++} and t_{--}) as well as cross-polarization (t_{+-} and t_{-+}) reflected/transmitted components due to polarization conversion of the chiral Au sawtooth metasurface. For RCP incident (beam 0) with unity amplitude $E_{0,+}$, the amplitudes for the transmitted and reflected beams (1 and 2) can be written as:

$$\boldsymbol{E}_1 = E_{1,+}\hat{a}_+ + E_{1,-}\hat{a}_- = [t_{++}^S\hat{a}_+ + t_{-+}^S\hat{a}_-] = [t_{++}\hat{a}_+ + t_{-+}\hat{a}_-], \tag{2a}$$

$$\boldsymbol{E}_2 = E_{2,+}\hat{a}_+ + E_{2,-}\hat{a}_- = \left\{\begin{Bmatrix} t_{-+}^S r_{+-}^G r_{++}^S \\ + \\ t_{++}^S r_{-+}^G r_{+-}^S \end{Bmatrix}\hat{a}_+ + \begin{Bmatrix} t_{++}^S r_{-+}^G r_{--}^S \\ + \\ t_{-+}^S r_{+-}^G r_{-+}^S \end{Bmatrix}\hat{a}_-\right\} * e^{-i2kL} = (r_{++}\hat{a}_+ + r_{-+}\hat{a}_-) * e^{-i(2kL+\phi_G)}, \tag{2b}$$

where $\hat{a}_\pm$ are unitary vectors for circular polarization, $r_{ij}^G = |r_{ij}^G|e^{-i\phi_G} = r_G e^{-i\phi_G}$ is the reflection coefficient for the top glass with amplitude r_G and phase $\phi_G = \pi$, $r_{++} = t_{-+}^S|r_{+-}^G|r_{++}^S + t_{++}^S|r_{-+}^G|r_{+-}^S$, and $r_{-+} = t_{++}^S|r_{-+}^G|r_{--}^S + t_{-+}^S|r_{+-}^G|r_{-+}^S$. Then the transmittance T_{RCP} can be calculated as:

$$\begin{aligned} T_{RCP} &= (\boldsymbol{E}_1 + \boldsymbol{E}_2)\cdot(\boldsymbol{E}_1 + \boldsymbol{E}_2)^* \\ &= \left(\left\{\begin{matrix} |t_{++}|e^{i\arg(t_{++})} \\ + \\ |r_{++}|e^{i\arg(r_{++})}e^{-i(2kL+\phi_G)} \end{matrix}\right\}\hat{a}_+ + \left\{\begin{matrix} |t_{-+}|e^{i\arg(t_{-+})} \\ + \\ |r_{-+}|e^{i\arg(r_{-+})}e^{-i(2kL+\phi_G)} \end{matrix}\right\}\hat{a}_-\right) \\ &\cdot\left(\left\{\begin{matrix} |t_{++}|e^{-i\arg(t_{++})} \\ + \\ |r_{++}|e^{-i\arg(r_{++})}e^{i(2kL+\phi_G)} \end{matrix}\right\}\hat{a}_+ + \left\{\begin{matrix} |t_{-+}|e^{-i\arg(t_{-+})} \\ + \\ |r_{-+}|e^{-i\arg(r_{-+})}e^{i(2kL+\phi_G)} \end{matrix}\right\}\hat{a}_-\right) \\ &= \left\{\begin{matrix} |t_{++}|^2 \\ + \\ |r_{++}|^2 \\ + \\ 2|t_{++}||r_{++}|\cos[2kL+\phi_G+\arg(t_{++})-\arg(r_{++})] \end{matrix}\right\} \\ &+ \left\{\begin{matrix} |t_{-+}|^2 \\ + \\ |r_{-+}|^2 \\ + \\ 2|t_{-+}||r_{-+}|\cos[2kL+\phi_G+\arg(t_{-+})-\arg(r_{-+})] \end{matrix}\right\}. \end{aligned} \tag{3}$$

Equation (3) can be further simplified into a two-beam interference form as:

$$T_{RCP} = |t_{++}|^2 + |r_{++}|^2 + |t_{-+}|^2 + |r_{-+}|^2 + 2\sqrt{u^2+v^2}\cos(2kL+\phi_G+\phi_{RCP}^S), \tag{4}$$

where u and v are functions of the transmission and reflection coefficients only, and

$$\phi_{RCP}^S = \arg(t_{++}) - \arg(r_{++}) + \delta_+, \tag{5a}$$

for δ_+ given as:

$$\delta_+ = \tan^{-1}\frac{|t_{-+}||r_{-+}|\sin\{[\arg(t_{-+})-\arg(r_{-+})]-[\arg(t_{++})-\arg(r_{++})]\}}{[|t_{++}||r_{++}|+|t_{-+}||r_{-+}|\cos\{[\arg(t_{-+})-\arg(r_{-+})]-[\arg(t_{++})-\arg(r_{++})]\}}. \tag{5b}$$

Here ϕ^S_{RCP} can be interpreted as the effective reflection phase for RCP incident light as measured in the experiment using a two-beam interference model. Similarly for LCP incidence with unity amplitude $E_{0,-}$, the transmittance of the glass-air-sawtooth etalon T_{LCP} and the phase ϕ^S_{LCP} can be obtained by changing the subscript indexes of t_{ij} and r_{ij} to opposite handedness, i.e. from + to − and vice versa, in Eqs. (3–5).

Figure 4D–F show the transmittance for LCP (red curves) and RCP (blue curves) incident light of the glass-air-sawtooth etalon calculated using Eq. (3) with reflection coefficient of the top glass $r_G = 0.2$ for the **N**-, **V**- and **И**-type complementary Au sawtooth metasurfaces respectively. The overall trends agree well with the simulated transmittance without the top glass shown in Figure 2E–G, and resemble well the results with the FP oscillations obtained in the experiment as shown in Figure 4A–C. However, in order to improve the accuracy in locating the peaks and troughs of the transmittance, we repeat the calculations using unphysical value for $r_G = 1$ (purple curves in insets of Figure 4D–F for RCP incident light) knowing that the positions of the peaks and troughs do not change as they are not sensitive to the amplitudes of the interference beams as indicated in the insets. We then obtain the reflection phase of the sawtooth metasurface by the same method used for the experiment above with the peaks/troughs of the transmittance obtained for $r_G = 1$. Figure 5E–G show the reflection phase with respect to Au film for LCP (red open circles) and RCP (blue open circles) incidence for the **N**-, **V**- and **И**-type Au sawtooth metasurfaces respectively. Note that data are a bit noisy around wave numbers ~1.48 μm^{-1} and ~1.65 μm^{-1} for the **N**- and **И**-type Au sawtooth metasurfaces because of large errors in the peak/trough positions due to large transmittance changes, see Figures 2E, G and 4D, F. Furthermore, there is a rapid phase increase from ~1.35 μm^{-1} to ~1.45 μm^{-1} for the **N**- and **И**-type Au sawtooth metasurfaces which is not observed in the experiment.

The reflection phase can also be calculated directly using Eq. (5) in the above and the results are shown as solid curves in Figure 5E–G for the **N**-, **V**- and **И**-type Au sawtooth metasurfaces respectively. The agreement with those obtained by fitting the peaks/troughs is very good, with the calculated results much smoother. This confirms our fitting method in finding the reflection phase from the FP peaks/troughs for the experiment. The reflection circular phase-dichroism, $\Delta\phi = \phi_{RCP} - \phi_{LCP}$, is shown in Figure 5H for the chiral **N**- and **И**-type Au sawtooth metasurfaces as well as the achiral **V**-type Au sawtooth metasurface. Despite larger values (~4 times the experimental results in Figure 5D) and also the zero circular phase-dichroism (crossings) at 1.57 μm^{-1} and 1.62 μm^{-1} observed only in the simulations but not in the experiments, the simulated circular phase-dichroisms are in qualitative agreement with the experiment. In particular, the maximum circular phase-dichroisms at ~1.39 μm^{-1} and ~1.61 μm^{-1} observed in the experiments correspond well to those at ~1.48 μm^{-1} and ~1.65 μm^{-1} in the simulations. Note also, that the simulated circular phase-dichroism results for the chiral **N**- and **И**-type Au sawtooth metasurfaces shown in Figure 5H are larger, ~4 times, than those obtained by the simulated CD results shown in Figure 2H, supporting strongly that circular phase-dichroism could be more sensitive than the conventional CD measurement for the characterization of chiral materials.

Note that the reflection phase of the sawtooth metasurface obtained using Eqs. (3–5) includes all transmitted polarizations. Due to the limitation of our present setup, this is exactly what was done in the experiment where both co-polarization and cross-polarization transmitted components were collected by the microscopic objective. It would be highly desirable to obtain separately, the reflection phases of both polarizations for any incident polarization in a reflection mode instead of the transmission mode used in our experiment as it could lead to better characterization of the Au sawtooth metasurfaces using the circular phase-dichroism approach and is planned for future experiments.

5 Conclusion

We propose a circular phase-dichroism approach using the reflection phase in the characterization of chiral materials. To demonstrate our approach we have fabricated planar complementary chiral Au sawtooth nanoarray metasurfaces and obtained circular phase-dichroism results that are comparable to the conventional CD measurements. We have also performed full-wave simulations of our chiral metasurface system and obtained good qualitative agreement with the experimental results. Importantly, our approach of using the reflection for the circular phase-dichroism provides a workable solution for the characterization of chiral metasurfaces when the transmission signal is too small for the conventional CD measurements. Our results demonstrate well, the potential of the circular phase-dichroism in sensing and metasurface characterizations.

Acknowledgments: W. Y. Tam acknowledges support from Hong Kong RGC grants AoE P-02/12 and C6013-18GF. X. Wang acknowledges support from the Key Research

and Development Program of Shandong Province (2018GGX101008) and the National NSFC (11874232). W. Y. Tam acknowledges support from the College of Mathematics and Physics at QUST. We thank Ho Ming Leung and Tsz Kit Yung for technical assistance.

References

[1] Kshetrimayum RS. A brief introduction to metamaterials. IEEE Potentials 2004;23:44–6.
[2] Engheta N, Richard WZ. Metamaterials: physics and engineering explorations. New York: John Wiley & Sons Inc, 2006.
[3] Zouhdi S, Sihvola A, Vinogradov AP. Metamaterials and plasmonics: fundamentals, modelling, applications. New York: Springer, 2008.
[4] Veselago VG. The electrodynamics of substances with simultaneously negative values of permittivity and permeability. Soviet Physics Uspekhi 1968;10:509–14.
[5] Pendry JB. Negative refraction. Contemp Phys 2004;45:191–202.
[6] Pendry JB. Negative refraction makes a perfect lens. Phys Rev Lett 2000;85:3966–9.
[7] Pendry JB, Schurig D, Smith DR. Controlling electromagnetic fields. Science 2006;312:1780–2.
[8] Shelby RA, Smith DR, Schultz S. Experimental verification of a negative index of refraction. Science 2001;292:77–9.
[9] Zhang X, Liu Z. Superlenses to overcome the diffraction limit. Nature Mater 2008;7:435–41.
[10] Schurig D, Mock JJ, Justice BJ, et al. Metamaterial electromagnetic cloak at microwave frequencies. Science 2006;314:977–80.
[11] Yen TJ, Padilla WJ, Fang N, et al. Terahertz magnetic response from artificial materials. Science 2004;303:1494–6.
[12] Huang LL, Chen XZ, Muhlenbernd H, et al. Dispersionless phase discontinuities for controlling light propagation. Nano Lett 2012;12:5750–5.
[13] Aieta F, Genevet P, Kats MA, et al. Aberration-free ultrathin flat lenses and axicons at telecom wavelengths based on plasmonic metasurfaces. Nano Lett 2012;12:4932–6.
[14] Allen L, Beijersbergen MW, Spreeuw RJC, Woerdman JP. Orbital angular momentum of light and the transformation of Laguerre-Gaussian laser modes. Phys Rev A 1992;45:8185–9.
[15] Padgett M, Courtial J, Allen L. Light's orbital angular momentum. Phys Today 2004;57:35–40.
[16] Yang YH, Wang HP, Yu FX, Xu ZW, Chen HS. A metasurface carpet cloak for electromagnetic, acoustic and water waves. Sci Rep 2015;6:20219.
[17] Slinger C, Cameron C, Stanley M. Computer-generated holography as a generic display technology. Computer 2005;38:46–53.
[18] Huang K, Gao HF, Cao GW, Shi P, Zhang XB, Li YP. Design of diffractive phase element for modulating the electric field at the out-of-focus plane in a lens system. Appl Opt 2012;51:5149–53.
[19] Hsiao HH, Chu CH, Tsai DP. Fundamentals and applications of metasurfaces. Small Methods 2017;1:1600064.
[20] Li A, Singh S, Sievenpiper D. Metasurfaces and their applications. Nanophotonics 2018;7:989–1011.
[21] Zhang L, Mei ST, Huang K, Qiu CW. Advances in full control of electromagnetic waves with metasurfaces. Adv Opt Mater 2016;4:818–33.
[22] Chen WT, Zhu AY, Sisler J, et al. Broadband achromatic metasurface-refractive optics. Nano Lett 2018;18:7801–8.
[23] Barron LD. Molecular light scattering and optical activity. Cambridge: Cambridge University Press, 2004.
[24] Lakhtakia A. Selected papers on natural optical activity. Wash: Spie Optical Engineering Press, 1990.
[25] Wang BN, Zhou JF, Koschny T, Kafesaki M, Soukoulis CM. Chiral metamaterials: simulations and experiments. J Opt A 2009;11:114003.
[26] Papakostas A, Potts A, Bagnall DM, Prosvirnin SL, Coles HJ, Zheludev NI. Optical manifestations of planar chirality. Phys Rev Lett 2003;90:107404.
[27] Vallius T, Jefimovs K, Turunen J, Vahimaa P, Svirko Y. Optical activity in subwavelength-period arrays of chiral metallic particles. Appl Phys Lett 2003;83:234–6.
[28] Kuwata-Gonokami M, Saito N, Ino Y, et al. Giant optical activity in quasi-two-dimensional planar nanostructures. Phys Rev Lett 2005;95:227401.
[29] Zhang W, Potts A, Bagnall DM. Giant optical activity in dielectric planar metamaterials with two-dimensional chirality. J Opt A 2006;8:878–90.
[30] Konishi K, Bai BF, Meng XF, et al. Observation of extraordinary optical activity in planar chiral photonic crystals. Opt Exp 2008;16:7189–96.
[31] Thiel M, von Freymann G, Wegener M. Layer-by-layer three-dimensional chiral photonic crystals. Opt Lett 2007;32:2547–9.
[32] Rogacheva AV, Fedotov VA, Schwanecke AS, Zheludev NI. Giant gyrotropy due to electromagnetic-field coupling in a bilayered chiral structure. Phys Rev Lett 2006;97:177401.
[33] Kanda N, Konishi K, Kuwata-Gonokami M. Terahertzwave polarization rotation with double layered metal grating of complimentary chiral patterns. Opt Exp 2007;15:11117–25.
[34] Decker M, Ruther M, Kriegler CE, et al. Strong optical activity from twisted-cross photonic metamaterials. Opt Lett 2009;34:2501–3.
[35] Decker M, Zhao R, Soukoulis CM, Linden S, Wegener M. Twisted split-ring-resonator photonic metamaterial with huge optical activity. Opt Lett 2010;35:1593–5.
[36] Gao WS, Ng CY, Leung HM, Li YH, Chen H, Tam WY. Circular dichroism in single layered gold sawtooth gratings. J Opt Soc Am B 2012;29:3021–6.
[37] Han CR, Leung HM, Tam WY. Chiral metamaterials by shadowing vapor deposition. J Opt 2013;15:072101.
[38] Han CR, Leung HM, Chan CT, Tam WY. Giant plasmonic circular dichroism due to electromagnetic couplings in Ag staircase nanostructures. Opt Exp 2015;23:33065–78.
[39] Knipper R, Mayerhöfer T, Kopecký Jr. V, Huebner U, Popp J. Observation of giant infrared circular dichroism in plasmonic 2D-metameaterial arrays. ACS Photonics 2018;5:1176–80.
[40] Oh SS, Hess O. Chiral metamaterials: enhancement and control of optical activity and circular dichroism. Nano Convergence 2015;2:24.
[41] Wang ZJ, Cheng F, Winsor T, Liu YM. Optical chiral metamaterials: a review of the fundametals, fabrication methods and applications. Nanotechnology 2016;27:412001.
[42] Zhu AY, Chen WT, Zaidi A, et al. Giant intrinsic chiro-optical activity in planar dielectric nanostructures. Light: Sci & Appl 2018;7:17158.
[43] Qiu M, Zhang L, Tang ZX, Wei J, Qiu CW, Lei DY. 3D metaphotonic nanostructures with intrinsic chirality. Adv Funct Mater 2018;28:1803147.

[44] Yung TK, Gao WS, Leung HM, Zhao QL, Wang X, Tam WY. Measurement of reflection phase using thick-gap Fabry-Perot etalon. Appl Opt 2016;55:7301–6.
[45] Zhao QL, Yung TK, Wang X, Tam WY. Correction of numerical aperture effect on reflection phase measurement using thick-gap Fabry Perot etalon. Appl Opt 2017;15:4392–7.
[46] Park J, Kang JH, Kin SJ, Liu XG, Brongersma ML. Dynamic reflection phase and polarization control of metasurfaces. Nano Lett 2017;17:407–13.
[47] Gao WS, Xiao M, Chan CT, Tam WY. Determination of Zak phase by reflection phase in 1D photonic crystals. Opt Lett 2015;40:5259–62.
[48] Gao WS, Xiao M, Chen BJ, Pun EYB, Chan CT, Tam WY. Controlling interface states in 1D photonic crystals by tuning bulk geometric phases. Opt Lett 2017;42:1500–3.
[49] Zhao QL, Liu J, Gao D, et al. Reflection phase of photonic bands in finite bi-directional 1D photonic crystals using effective medium approach. OSA Continuum 2018;1: 332–9.
[50] Feng TH, Liu F, Tam WY, Li J. Effective parameters retrieval for complex metamaterials with low symmetries. EPL 2013;102:18003.
[51] Leung HM, Han CR, Li YH, Chan CT, Tam WY. Modeling quasi-3D chiral metamaterials fabricated by shadowing vapor deposition. J Opt 2014;16:015102.
[52] Ghosh G. Dispersion-equation coefficients for the refractive index and birefringence of calcite and quartz crystals. Opt Communications 1999;163:95–102.
[53] Kasarova SN, Sultanova NG, Ivanov CD, Nikolov ID. Analysis of the dispersion of optical plastic materials. Opt Mater 2007;29:1481–90.

Article note: Ranran Zhang is a PhD student at the Physics Department of the College of Mathematics and Physics, Qingdao University of Science and Technology (QUST). This project was under the joint supervision of Prof. X. Wang at QUST and Prof. W. Y. Tam at the Hong Kong University of Science and Technology (HKUST).